SIMULATION OF CREEP IN MICRON SCALE CRYSTALLINE MATERIALS FOR HIGH TEMPERATURE THERMAL PROTECTION SYSTEMS

A Thesis

by

CHRISTOPHER ALDEN GREER

Submitted to the Office of Graduate and Professional Studies of
Texas A&M University
in partial fulfillment of the requirements for the degree of

MASTER OF SCIENCE

Chair of Committee,	Amine Benzerga
Committee Members,	Paul Cizmas
	John Whitcomb
	Miladin Radovic
Head of Department,	Rodney Bowersox

May 2016

Major Subject: Department of Aerospace Engineering

ABSTRACT

The use of thermal barrier coatings over the past few decades has significantly improved the performance of gas turbine engines by reducing the operating temperature of engine components. However, these multilayer systems are not able to be used to their full potential due to the difficulty of accurately modeling the complex interplay of physical phenomena, such as creep and oxidation, that contribute to failure. In order to address this issue, more physics-based failure prediction models need to be developed. One potential way to do this is through the use of dislocation dynamics (DD) models. A DD framework was recently developed which incorporates high temperature effects such as vacancy diffusion assisted dislocation climb in addition to dislocation glide. However, the effects of certain parameters on simulations of dislocation creep had been unexplored. In particular, the effect of the distance required for a dislocation to climb to a new slip plane, the critical climb distance, was not evaluated and the vacancy relaxation volume was set at zero, negating its effect on the calculation of vacancy diffusion. The present work aims to address this by studying the effect of the critical climb distance and the vacancy relaxation volume on the creep response of micron scale single crystals. The critical climb distance was found to have an approximately inversely proportional effect on the steady state creep rate, but did not affect the stress dependence of the creep rate, while the use of a nonzero vacancy relaxation volume was found to have a slight effect on both the steady state creep rate and the stress dependence of the creep rate. Furthermore, the use of a nonzero vacancy relaxation volume introduced the effect of the pressure gradient into the vacancy diffusion simulation.

ACKNOWLEDGEMENTS

First, I would like to thank my parents for their unfailing love, support, and encouragement throughout my graduate studies. I would also like to thank my advisor, Dr. Amine Benzerga for for assisting me with my research, as well as my committee for their time and support. Additionally, I would like to thank the past and present members of Dr. Benzerga's research group for their support and assistance, particularly Babak Kondori, whose technical expertise and assistance have proven invaluable. Finally, I would like to thank the Texas A&M University Department of Aerospace Engineering staff, particularly Karen Knabe, Miriam Brown, and Ashley Brown for their timely assistance with advising, coordinating, and scheduling.

TABLE OF CONTENTS

Page

LIST OF FIGURES

FIGURE Page

LIST OF TABLES

TABLE Page

CHAPTER I

INTRODUCTION

I.1 Motivation

Over the past several decades, the performance of gas turbine engines has been significantly improved through the use of thermal barrier coatings (TBCs). Because of their low thermal conductivity, TBCs reduce the temperature of components to which they are applied by over 100°C. When combined with various cooling methods, a temperature reduction of over 250°C can be achieved [15]. This provides two benefits. First, a higher combustion temperature can be reached without melting engine components, which results in greater thermodynamic efficiency. Alternatively, the combustion temperature can be kept the same while the operating temperature of the coated components is reduced, which affords an increase in their service life.

TBC systems are composed of layers of several materials, which are shown in Figure I.1. The first layer is the substrate, which is the component to which a TBC system is applied, such as a superalloy turbine blade. The bond coat layer is an aluminum containing alloy which is applied to the substrate and helps protect it from corrosion and oxidation. The next layer is the thermally grown oxide (TGO), which forms as oxygen combines with the aluminum in the bond coat to create α-Al_2O_3 [13, 34]. This layer grows throughout the life of the TBC system, and this growth can contribute to eventual failure of the system. The final layer is the ceramic top coat, which provides most of the thermal insulation and impact resistance for the TBC.

Despite the benefits provided by TBC systems, they are not currently used to their full potential in engine design since accurate lifetime prediction remains a diffi-

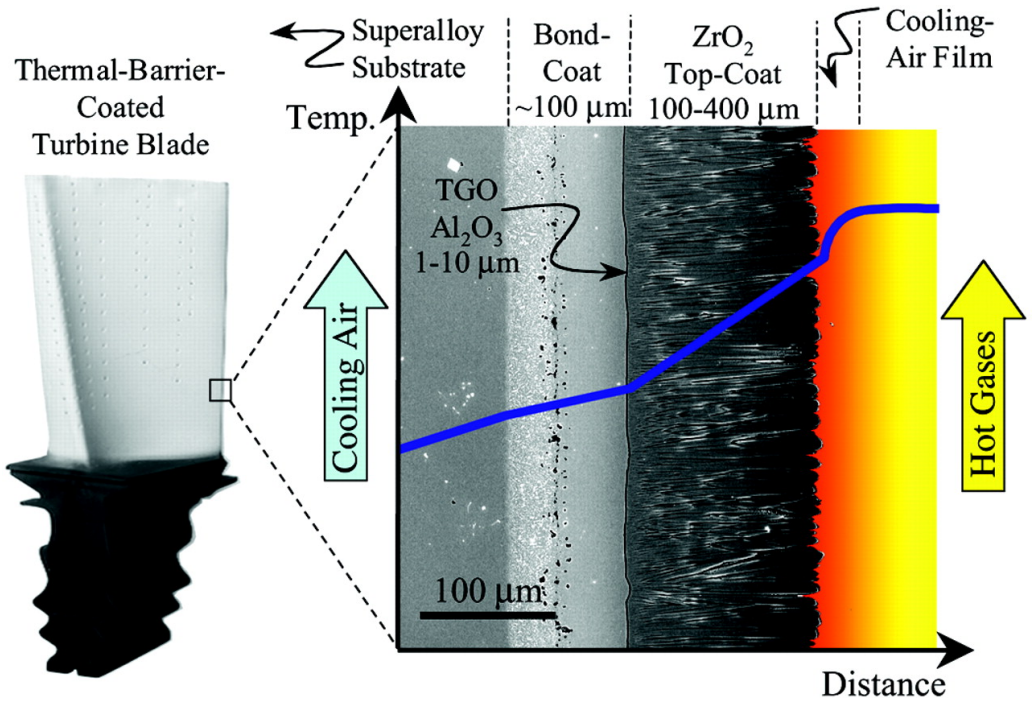

Figure I.1: A cross-section of a TBC with an EB-PVD top coat applied to a turbine blade, reprinted with permission from [34].

cult problem [15]. A model of the evolution of stress and strain resulting from thermal cycling throughout the life of a TBC has been developed by Balint and Hutchinson, which is widely used at both research institutions, such as ONERA (the French aerospace research organization), and engine manufacturers, such as Rolls-Royce and General Electric. In this model, each layer of the TBC is modeled individually with its own constitutive equations [3, 4]. The strain of the bond coat and top coat are both characterized by power law creep equations of the form $\dot{\epsilon}_R \propto \sigma_R^n$, with a reference creep stress $\dot{\epsilon}_R$, reference creep strain σ_R, and creep exponent n obtained from experiments. The TGO is modeled as elastic/perfectly plastic, with a growth strain rate given by

$$\dot{\varepsilon}_G = \frac{\dot{h}}{d} \tag{I.1}$$

where $\dot{h}$ is thickening rate of the oxide and d is a fitting parameter [4]. Although this model has enhanced the understanding of rumpling in TBCs, there are a few questionable aspects. First, a **size dependence** of material properties exists for crystalline materials. Experiments have shown that the mechanical properties of metals several microns thick or smaller differ greatly from the bulk material [16, 17]. Therefore, given the micron or even submicron thicknesses involved, the properties of the bond coat, TGO, and possibly the top coat, may not be accurately obtained from experiments on bulk material. Size effects also mean that the use continuum models of plasticity in layers less than a micron thick may not be valid. Additionally, the constant d in equation I.1 is an **empirical** factor chosen to maintain a constant growth rate for the TGO. However, given the potential variation of the physical processes that cause TGO growth, it is important to elucidate the relationship between the factor d and various microstructural factors such as grain size, dislocation mobility, etc. A solution to this would be to incorporate more physics into these aspects of TBC models.

I.2 Objective

The **broad goal** of this research is the development of physics-based models of plasticity mediated damage in TBCs. One step toward this goal is to investigate the creep response in unconfined micron-scale volumes, which constitutes the **main research objective** of this thesis.

A particularly promising approach for accomplishing this is through the use of a discrete dislocation dynamics (DD) model which simulates the movement of dislocations in a material through both glide and climb. Such a method is well suited to modeling the creep of the bond coat, since creep at high homologous temperatures and moderate stresses is due to a combination of both climb and glide of dislocations.

Additionally, it might be used to model the growth of the TGO, since this can be modeled as the insertion of planes of atoms due to dislocation climb as the oxygen and aluminum ions diffuse through the oxide as shown in Figure I.2 [7].

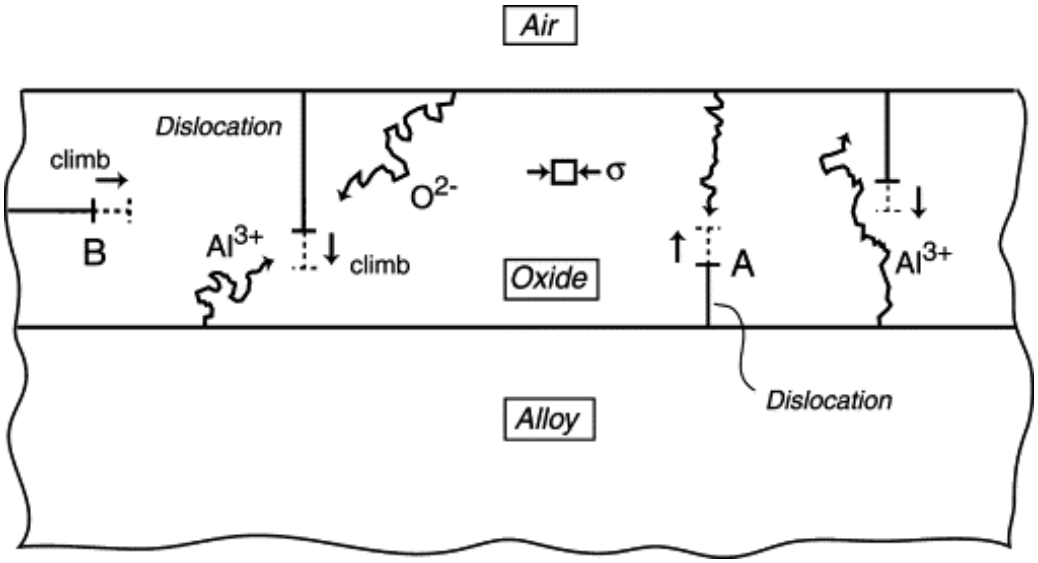

Figure I.2: Illustration of oxide growth due to diffusion, reprinted with permission from [7].

Recently, a computational framework was developed which incorporates both the glide and climb of dislocations, enabling the behavior of crystalline materials at high homologous temperatures to be simulated [26, 27]. This is possible through separation of the glide and climb processes, a fact which greatly simplifies the simulation process since vacancy diffusion occurs over a much larger time scale than glide. The framework has been successfully used to simulate power law creep in single crystals [26, 27]. However, this simulation framework involves various parameters. Some of these are physically meaningful, such as the vacancy relaxation volume; others are merely algorithmic, such as the critical distance for climb in the staggered approach

of time scale separation. How these parameters affect the predicted response has yet to be explored. The **specific objective** of the thesis is to examine the effects of physical as well as algorithmic parameters on the creep response of micron scale layers of crystalline material.

CHAPTER II

BACKGROUND

In order to further clarify the connection between TBC failure, creep, and dislocation dynamics, some background on each topic is given in this chapter.

II.1 TBC Systems and Failure Mechanisms

As mentioned in Section I.1, TBC systems are composed of several layers of various materials which exhibit different behavior during operation. An illustration of these layers is shown in Fig. I.1. The first layer of the TBC system is the substrate which is the component to which a TBC system is applied. It is typically composed of a nickel or cobalt based superalloy plus a few other alloying elements [34]. The bond coat layer is applied to the substrate and is between 40 μm and 100 μm thick [15]. It serves to protect the substrate from oxidation and corrosion and influence the growth and development of the oxide that forms the next layer of the system. There are two main types of bond coat. The first is an alloy of either NiCrAlY or NiCoCrAlY which is applied to the substrate with either the electron beam physical vapor deposition (EB-PVDa) or low pressure plasma spray technique [15, 34]. The second type is a platinum-modified diffusion aluminide in which a layer of platinum is electroplated onto the substrate and and then diffusion aluminized [13, 15, 34]. As the system undergoes thermal cycles during its lifetime, the thermally grown oxide (TGO) layer forms on top of the bond coat. Approximately 1-10 μm thick, this layer provides additional protection against oxidation and binds the bond coat to the ceramic top coat, which is the final layer of the TBC system [13, 34]. α-Al_2O_3 serves both of these purposes well, so bond coats are designed with sufficient Al to make this the primary oxide that forms as oxygen diffuses through the top

coat. Since the TGO holds the bond coat and top coat together and grows and evolves throughout the service life of the system, it can play a critical role in TBC failure. Several factors affect the integrity of the TGO. Stresses may develop in the TGO due to thermal expansion mismatches among the TBC layers and growth of the oxide. Additionally, defects such as voids and microcracks may develop and the diffusion of various elements, such as sulfur, from the other TBC layers can adversely affect the TGO cohesion [15]. The final layer is the ceramic top coat, which provides most of the thermal insulation and impact resistance for the TBC. This layer is usually composed of zirconia stabilized with yttria (YSZ) since it has several desirable properties. It has a high coefficient of thermal expansion, which helps to accommodate the thermal expansion of the other layers, a very low thermal conductivity at high temperatures, and a melting point of around 2700°C, making it a particularly good choice for high temperature applications. YSZ also provides good protection against other environmental factors with good corrosion resistance and a hardness of around 14 GPa [34]. Additionally, its low density means that its use does not add a lot of weight, a particularly important consideration for aeronautical applications. There are two methods for applying the ceramic top coat: air plasma spraying (APS) and electron beam physical vapor deposition (EB-PVD). The APS method creates a thicker coating (around 300 μm) with cracks parallel to the surface and 15 to 25 vol% porosity, both of which further decrease thermal conductivity and elastic modulus [34]. Another feature of APS tops coats is that they require a rough undulating interface with the bond coat to improve adhesion, although this produces out of plane stresses that can grow during service and eventually cause failure. EP-BVD top coats, on the other hand, are thinner (around 125 μm) and can be deposited onto a smooth bond coat surface. This method results in a microstructure of equiaxed grains near the interface, followed by a region of columnar grains that extends to the

surface of the top coat. This imparts more strain tolerance than the APS method, but does not provide as great a reduction in thermal conductivity. EP-BVD top coats are also less likely to build up over and close the cooling holes on turbine airfoils, but are more expensive than APS top coats [15].

The failure of TBC systems is manifested in the cracking and spallation of one or more layers. The mechanisms by which this occurs can be divided into two categories: extrinsic and intrinsic. Extrinsic failure mechanisms are those in which failure is due to foreign particles. One such mechanism is foreign object damage (FOD), whereby particles in the gas stream impact the TBC coated component and cause erosion of the top coat. APS top coats are more susceptible to this than EP-BVD ones due to the presence of cracks parallel to the interface with the TGO [35]. Particles can also collect on the surface and melt, penetrating the top coat. This increases the stiffness of the top coat, thus reducing its strain tolerance, which can cause delamination upon cooling due to thermal expansion mismatch. This failure mechanism is called "cold shock delamination" [15].

Intrinsic failure mechanisms are ones which occur as a result of the behavior of the constituents of the TBC system. As the TBC system is subjected to operating conditions, cracks develop due to thermal expansion mismatch stresses, growth stresses due to growth of the TGO, and imperfections which can serve as nucleation sites for cracks. The thermal mismatch stresses arise due to the fact that the TGO has a smaller thermal expansion coefficient than the bond coat and top coat layers [13]. This leads to stresses upon heating of the system, which relax through creep at high temperatures and during cooling. Due to the strain tolerance of the top coat, these stresses are greatest at the bond coat/TGO interface. As the TGO oxidizes, it experiences growth strains in both the lateral and normal directions. The normal growth strains result in thickening of the TGO and cause rigid body displacements

for a planar TGO. The lateral growth strains, on the other hand, arise from oxidation on grain boundaries normal to the interface. This causes compressive in-plane stresses in the TGO. Although the growth stresses are typically smaller than thermal expansion mismatch stresses (0-1 GPa vs. 3-4 GPa), they can become much larger near imperfections and contribute to failure [13]. One type of imperfection is the segregation of elements such as W, Ta, and Re from the substrate along grain boundaries to the TGO [15]. This reduces the adhesion of the TGO. Another source of imperfections is the depletion of Al in the bond coat, leading to the formation of other oxides besides α-Al_2O_3 and weakening the TGO. Imperfections in the surface geometry of the interface between the bond coat and TGO or between the TGO and the top coat may also contribute to failure by causing out-of-plane stresses. For TBC systems with APS top coats, the rough surface required for application of the top coat means that these imperfections exist from the beginning. TBC systems with EP-BVD top coats can develop undulations as a result of stresses in the TGO and relaxation by creep over the course of several thermal cycles. Finally, TGO thickness imperfections may arise in areas with higher O^{-2} diffusivity [13].

The predominant intrinsic failure mechanisms for TBC systems vary depending on whether they are used in power generation applications, which involve long periods at high temperature and relatively few thermal cycles, or aviation applications, which involve repeated thermal cycles. For TBC systems subjected to low thermal cycling typical in power generation, failure is driven by TGO growth stresses. As the TGO grows around imperfections at high temperatures, compressive stresses arise normal to the interface, while tensions tangential to the interface develop in the top coat, potentially causing cracks to nucleate. The bond coat may also creep in response to TGO growth stresses. These compressive stresses decrease during cooling due the the top coat's higher coefficient of thermal expansion, becoming tensile if the bond coat

experienced enough creep and possibly causing interfacial cracking. Additionally, the thermal expansion misfit increases the tangential tension in the top coat upon cooling, which can lead to further crack nucleation and propagation. The cracks in the top coat and interface can coalesce and cause spallation of the top coat. In this way, both TGO growth and thermal expansion misfit lead to failure around imperfections [13].

For TBC systems used in aviation, the primary failure mechanism is a cyclic phenomenon termed ratcheting or rumpling, an example of which is shown in II.1. At high temperature, the lateral growth of the TGO induces a compressive stress in the oxide. This stress is relieved through out-of-plane displacements initiated at pre-existing undulations and plastic deformation of the bond coat. At the same time, the compressive stress in the TGO increases until it yields, at which point the TGO only grows through thickening [24]. During cooling, the thermal expansion misfit plus the TGO growth strain creates tensile stresses in the bond coat and compressive stresses in the TGO. Once these stresses reach the yield strength of the bond coat, it flows from the valleys to the peaks of undulations, enabling further increases in amplitude [13]. Upon reheating, the thermal expansion misfit reduces the stresses and the amplitude of the undulations is somewhat diminished [24]. The process then repeats with the undulations growing with each cycle. It is important to note that if the undulation growth were only due to the thermal mismatch stress, then after several cycles the process would reach an equilibrium where the amplitude does not increase with each additional cycle. However, the lateral growth strain of the TGO with each cycle sustains continued undulation growth [13]. As the undulations in the TGO increase in amplitude, the valleys penetrate into the relatively soft bond coat, which induces tensile stresses in the top coat normal to the interface, initiating cracks that eventually lead to spallation of the top coat [13]. Such cracking can be seen in

Fig. II.1. Predicting this type failure is a major motivator for the development of lifetime prediction models.

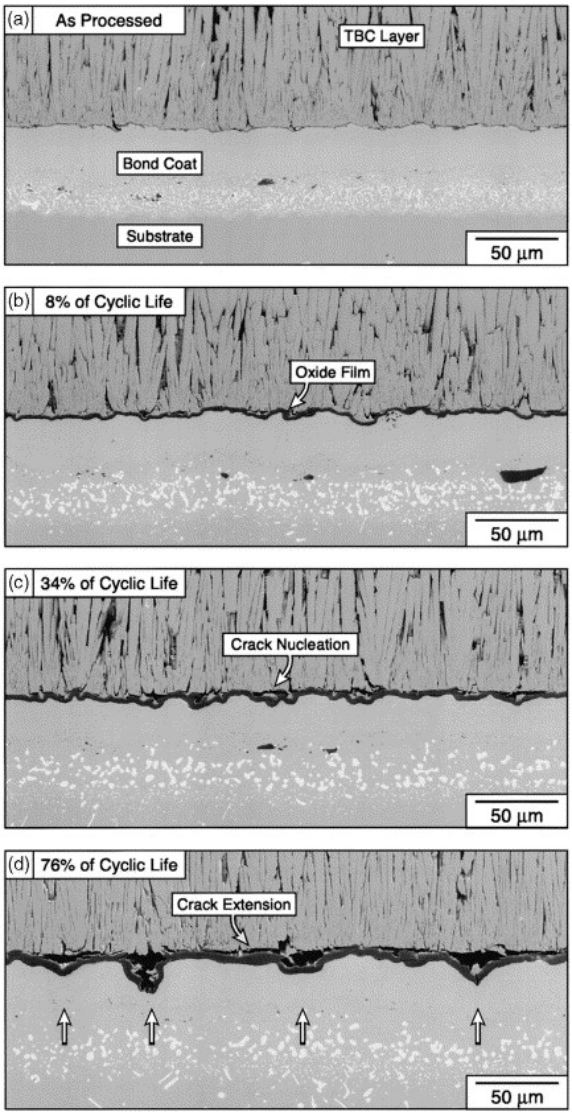

Figure II.1: Cross-sections of a TBC as rumpling occurs during thermal cycling, reprinted with permission from [32].

II.2 Creep

Typically when a load is applied at low homologous temperatures, crystalline materials exhibit little to no plasticity until the yield stress is reached. At higher temperatures and over longer time periods, however, crystalline materials experience plastic deformation at stresses below the yield stress in a phenomenon called creep. When a constant stress is applied to a material, the strain versus time follows the general profile shown in figure II.2 [27]. After an initial nearly instantaneous strain to ϵ_0, the strain rate decreases with time in what is called stage I creep. The strain rate then reaches a steady-state which is referred to as stage II creep. The strain rate during this stage is the called the minimum creep rate, which is used as a design parameter for a material. Finally, in stage III creep, the strain rate increases with time until the specimen fractures. It is important to note that this numbering system is the one used in the United States and is not universal. In Britain, the initial instantaneous strain is designated as the first stage, for a total of four stages of creep [12]. The specific mechanisms by which creep occurs depend on the homologous temperature and the applied stress normalized by the shear modulus, σ/μ. At relatively high stresses, $\sigma/\mu > 10^{-2}$, deformation occurs primarily through dislocation glide. Dislocation creep occurs at stresses in the range of $10^{-4} < \sigma/\mu < 10^{-2}$. In this mechanism, most of the strain occurs through dislocation glide, but vacancy diffusion enables dislocations to climb and overcome obstacles [39, 41]. This is the primary creep mechanism simulated in the framework used in this study. At low stresses, $\sigma/\mu < 10^{-4}$, creep takes place through the movement of vacancies and interstitials due to an applied stress [12]. Diffusion within individual grains predominates at high homologous temperatures, as atoms flow from boundaries under normal compression to those under normal tension, accompanied by the corresponding flow of vacancies

in the opposite direction [12, 21]. This is called Nabarro-Herring creep. At lower temperatures, on the other hand, diffusion occurs primarily along grain boundaries in a process known as Coble creep [12, 9].

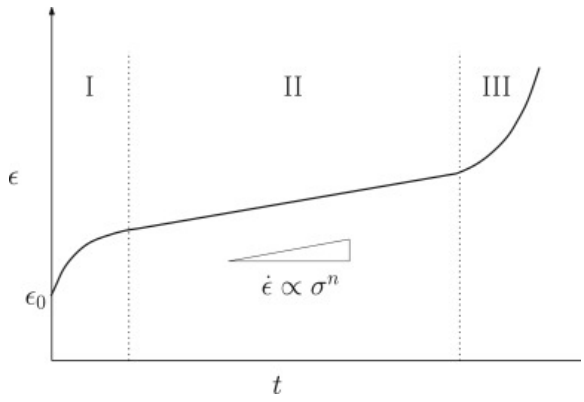

Figure II.2: Illustration of the three stages of creep exhibited by a material subjected to a constant stress, reprinted with permission from [27].

The dependence of the steady-state creep rate on the applied shear stress is often given as a power law relation of the form

$$\dot{\varepsilon} \propto \tau^n \bar{d}^{-p} \tag{II.1}$$

where τ is the applied shear stress and $\bar{d}$ is average grain size [26, 27]. The constant of proportionality is determined by various microstructural variables and constants used to obtain a fit to experimental data, which vary according to the specific mechanisms being modeled and the model being used. n and p are exponents governing the dependence on shear stress and grain size, respectively, and also depend on the specific creep mechanism. In the model for Nabarro-Herring creep, for example, $n = 1$ and $p = 2$ [12, 9, 21]. $n = 1$ as well for Coble creep while $p = 3$ [12,

9]. There is no grain size dependence for dislocation creep, however n can vary considerably depending on the applied shear stress. At stresses below $\tau/\mu \approx 10^{-6}$, $n = 1$. Although this linear dependence on stress occurs at low stress just as diffusion creep, dislocation creep mechanisms are still believed to operate in what is called Harper-Dorn creep [20]. Between $\tau/\mu \approx 10^{-6}$ and $\tau/\mu \approx 10^{-3}$, n falls within a range of 3-8, with experiments by Weertman and others showing a value between 4 and 5 for aluminum [40, 41]. At stresses above $\tau/\mu \approx 10^{-3}$, the creep rate increases at an even higher rate with stress. This is known as power law breakdown [12, 43]. An illustration of this is shown in figure II.3.

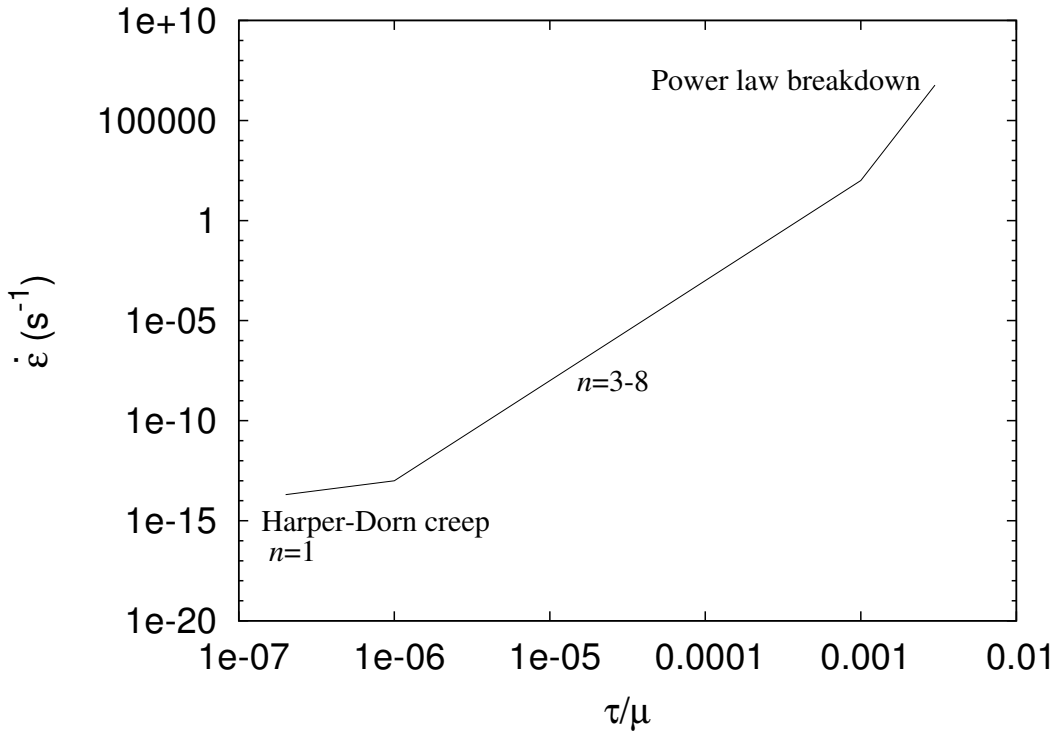

Figure II.3: Illustration of the effect of stress on the value of n.

Although the creep behavior of bulk materials is well documented, the behavior

at micron and submicron scales has been found to differ. For example, compressive creep experiments on micron scale aluminum columns by Ng and Ngan revealed lower steady-state creep rates than for bulk material, accompanied by periodic "strain bursts" [33]. Both the creep rates and the frequency of strain bursts varied from sample to sample, appearing to be stochastic in nature. Additionally, compression and tension experiments on nano- and micro-scale samples of various metals have shown that yield strength and hardening depend on sample size [17, 16]. This size effect is often attributed to the idea, based on observations, that the number and position of dislocations can vary significantly between specimens at the nano- and micro-scale, whereas for a bulk material, enough dislocations are present to assume a constant density and distribution. Furthermore, the smaller scales make it easier for dislocations to become annihilated at free surface, causing a fluctuation in their density. Creep experiments of thin films have also shown a deviation from the creep behavior of bulk materials [6, 22]. Hirakata et al. documented an increase in the creep rate of aluminum thin films as the thickness decreased to 400-200 μm, but a decrease in the creep rate with further decreases in thickness [22]. These effects have been explained as the result of increased diffusion along grain boundaries due to the increase in grain boundary area as volume decreases. However, as the specimen size decreases, the effect of surface tension increases, impeding creep. It is clear that the specimen size and variation in microstructure must be taken into account in order to properly model creep at nano- and micro-scales. Classic creep equations which fail to account for specimen size are unable to do this, but dislocation dynamics models have the potential to do so.

II.3 Dislocation Dynamics

Dislocation dynamics essentially forms a bridge between continuum plasticity used for large scales, and molecular dynamics, which is only practical at very small scales near the atomic level. In dislocation dynamics, the dislocation defects within a crystal and their interactions are modeled. Since dislocations are the primary carriers of plasticity, this enables the physics of plastic phenomena to be simulated in a more fundamental way than the empirical equations upon which classical plasticity is based. This makes it well suited to simulating plasticity at nano- and micro-scales where the behavior does not follow empirical relations. However, molecular dynamics frameworks explicitly model every atom in a system, making the simulation of micron scale specimens over short time periods computationally demanding, and impractical over longer time periods such as those involved in creep. Dislocation dynamics approaches, on the other hand, only model the defects within a material, making them much more practical to use from a computational standpoint.

In order to better understand how various aspects of plastic deformation are related to the behavior of dislocations, dislocation dynamics models began to be developed in the 1980's and early 1990's [11, 2, 29, 30]. Although these early models used relatively simple rules to govern dislocation behavior, DD models have become increasingly complex. Generally, there are two basic types of DD models: 2 dimensional and 3 dimensional. In 2D models, dislocations are represented as straight line defects that are restricted to motion in two dimensions. Dislocation sources and obstacles are treated as static objects which produce or release pinned dislocations depending on whether a critical stress has been reached. This somewhat simplified representation allows for larger strains and simulation times to be reached, but fails to fully account for 3 dimensional effects such as the formation of dynamic sources

and obstacles. While more computationally intensive, 3D DD models can allow a more precise simulation of dislocation interactions. Dislocations are modeled as dislocation loops or pinned line segments and allowed to move within a 3 dimensional crystal along defined slip planes or climb between them. Dynamic junction formation and destruction is possible, enabling the density of sources and obstacles to vary throughout the course of a simulation, which allows for the simulation of phenomena such as hardening. In addition to 2D and 3D models, a hybrid "2.5D" model has been developed by Benzerga et al., which incorporates some 3D mechanisms into a 2D framework [5]. Although not as computationally demanding as a 3D model, the 2.5D approach has extended the range of problems that can be simulated with 2D models. Since the development of DD, various frameworks have been created and modified in order to model and investigate several aspects of crystal plasticity such as crack tip plasticity and crack growth, work hardening at small scales, and creep [1, 10, 8, 19, 27, 18, 28, 31, 42].

Prior to the model used in this work, several DD models had been used to simulate creep, incorporating varying degrees of physics. In one of the earliest 2D models, created by Lepinoux and Kubin, glide and climb of dislocations is governed by whether the applied stress on a dislocation exceeds resistive stresses in the glide and climb directions [30]. Adjustment of theses resistive stresses determines the ease with which glide or climb occur, without directly incorporating the physical parameters that determine these processes, such as temperature. Another 2D model used by Miguel et al. to simulate the transition from stage I to stage II creep as a result of dislocation jamming, accounts for the effect of temperature on dislocation glide, but does not include the dislocation climb, which is believed to be a critical feature of high temperature creep [31]. More recently, a 3D model was used to simulate high temperature creep in nickel based superalloys [19]. While the dislocation interac-

tions were more accurately simulated than in previous creep simulations, the effect of variables such as temperature on dislocation climb were accounted for using a heuristic glide-to-climb mobility ratio which is adjusted based on the intended simulated temperature. Additionally, because of the long computation times required for 3D DD simulations, drag coefficients were used which are much lower than those in real materials, resulting in higher strain rates than in real creep experiments. In an effort to create a more physics-based DD framework for high temperature creep, the model of van der Giessen and Needleman was extended by Keralavarma to include the effect of vacancy diffusion on dislocation climb [26, 27]. This is the model which is used in the present work, and the details of the formulation are provided in the subsequent chapters.

CHAPTER III

MULTISCALE MODELING APPROACH AND IMPLEMENTATION

This section contains a description of the dislocation dynamics formulation developed by Van der Giessen and Needleman [11] and extended to include dislocation climb by Keralavarma [26]. An elastic body V containing N edge dislocations is postulated. The body is subjected to both displacement and traction boundary conditions and calculation of the resulting elastic fields is discussed below.

III.1 Superposition Method

The elastic fields arise from both the imposed boundary conditions on the body and the presence of dislocations within it. In order to solve for these fields, the superposition method is used to break them down into the fields created by the presence of the discrete dislocations in an infinite medium, denoted by ($\tilde{}$), and the complementary fields that enforce the boundary conditions of the problem, denoted by($\hat{}$). Thus, the total stresses strains and displacements are the sums of these two fields:

$$\boldsymbol{\sigma} = \tilde{\boldsymbol{\sigma}} + \hat{\boldsymbol{\sigma}}, \quad \boldsymbol{\epsilon} = \tilde{\boldsymbol{\epsilon}} + \hat{\boldsymbol{\epsilon}}, \quad \mathbf{u} = \tilde{\mathbf{u}} + \hat{\mathbf{u}} \tag{III.1}$$

where $\boldsymbol{\sigma}$, $\boldsymbol{\epsilon}$, and $\mathbf{u}$ are the stresses, strains, and displacements, respectively. The fields for each dislocation i can be be calculated analytically [23] and then summed to compute the ($\tilde{}$) fields:

$$\tilde{\boldsymbol{\sigma}} = \sum_{i=1}^{N} \boldsymbol{\sigma}^i, \quad \tilde{\boldsymbol{\epsilon}} = \sum_{i=1}^{N} \boldsymbol{\epsilon}^i, \quad \tilde{\mathbf{u}} = \sum_{i=1}^{N} \mathbf{u}^i \tag{III.2}$$

The ($\hat{}$) fields are subject to the following governing equations:

$$\hat{\boldsymbol{\epsilon}} = \frac{1}{2}\left(\nabla\hat{\mathbf{u}} + \nabla\hat{\mathbf{u}}^T\right), \quad \nabla\cdot\hat{\boldsymbol{\sigma}} = \mathbf{0}, \quad \hat{\boldsymbol{\sigma}} = \mathbf{C} : \hat{\boldsymbol{\epsilon}} \tag{III.3}$$

where $\mathbf{C}$ is the elasticity tensor. The boundary conditions resulting from the imposed tractions and displacements are:

$$\hat{\boldsymbol{\sigma}}\cdot\mathbf{n} = \mathbf{t}_0 - \tilde{\boldsymbol{\sigma}}\cdot\mathbf{n} \quad \text{on } \partial V_t, \qquad \hat{\mathbf{u}} = \mathbf{u}_0 - \tilde{\mathbf{u}} \quad \text{on } \partial V_u \tag{III.4}$$

where ∂V_t and ∂V_u are the parts of the domain boundary to which the tractions, $\mathbf{t}_0$, and displacements, $\mathbf{u}_0$ are applied.

III.2 Time scale separation

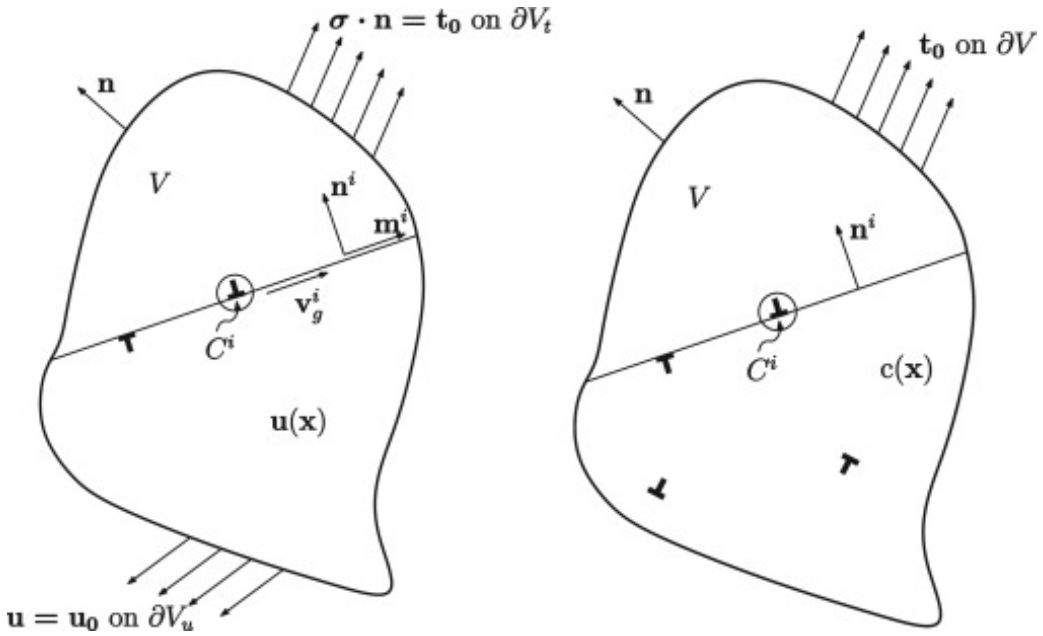

Figure III.1: Illustration of the boundary value problems for both dislocation glide (left) and climb (right), reprinted with permission from [27].

Dislocation glide and climb take place over vastly different time scales. Except at very high homologous temperatures, glide velocities are several orders of magnitude higher than climb velocities. Thus, simulating both in a computationally efficient manner is challenging. The framework presented here resolves this by separating the glide and climb processes. The boundary value problem for each is shown in Figure III.1. This is possible due to the concept of a "quasi-equilibrium" state in a system containing many dislocations. When dislocation glide is simulated at applied stresses below the yield stress, the strain rate approaches zero as dislocation glide activity becomes reduced through annihilation or pinning at obstacles. This happens within a much shorter time frame than the climb process. In light of this, dislocation glide is simulated until the quasi-equilibrium state is reached, at which point the dislocations are frozen on their slip planes and the climb process is started. Once a climb event is detected, simulation of climb ceases and dislocation glide resumes. In this way, creep occurs as diffusion assisted climb enables glide to resume each time a quasi-equilibrium state is reached. It is important to note that dislocation glide never completely ceases in reality, but that the glide process is terminated when the overall strain rate falls below a certain threshold.

III.3 Climb Formulation

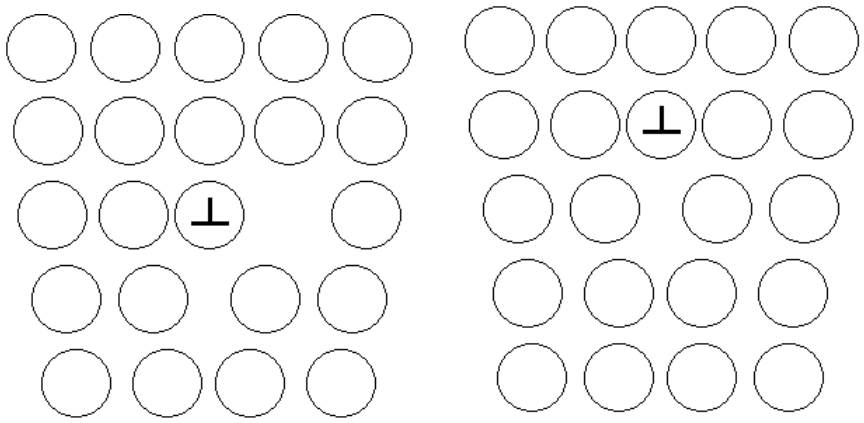

(a) (b)

Figure III.2: Illustration of positive climb of a dislocation through the absorption of a vacancy.

Dislocation climb occurs via the absorption and and emission of vacancies. The absorption of a vacancy results in the positive climb of a dislocation as shown in figure III.2, while the emission of a vacancy results in negative climb. The two factors that drive dislocation climb are the Peach-Koehler force and the gradient of the chemical potential of vacancies between a dislocation and the surrounding matrix. The Peach-Koehler force is a configurational force due to the stress fields created by each dislocation in the medium, $\tilde{\boldsymbol{\sigma}}$, and the stress fields which enforce the boundary conditions, $\hat{\boldsymbol{\sigma}}$, acting on a dislocation. The equation for the Peach-Koehler force on dislocation i is given by the equation from Van der Giessen and Needleman [11]:

$$\mathbf{f}^i = \mathbf{t}^i \times \left[\left(\hat{\boldsymbol{\sigma}} + \sum_{j \neq i} \boldsymbol{\sigma}^j \right) \cdot \mathbf{b}^i \right] \tag{III.5}$$

where $\mathbf{b}^i$ is the Burgers vector and $\mathbf{t}^i$ is the unit vector tangent to the dislocation line. This force can be decomposed further into a glide component, f_g, and a climb component,f_c:

$$\mathbf{f}^i = f_g^i \mathbf{m}^i + f_c^i \mathbf{n}^i \tag{III.6}$$

where $\mathbf{n}^i$ is the normal vector to the slip plane and $\mathbf{m}^i = \mathbf{t}^i \times \mathbf{n}^i$. The gradient of the chemical potential of vacancies drives the diffusion of vacancies which enables dislocation climb. The chemical potential for vacancy self-diffusion is given by:

$$\mu_v = \frac{kT}{\Omega}\left[\frac{E_f}{kT} - \frac{p\Omega_v}{kT} + \log\frac{c}{(1-c)}\right] \tag{III.7}$$

where k is the Boltzmann constant, T is the absolute temperature, Ω is the atomic volume, E_f is the formation energy of a vacancy, p is pressure, Ω_v is the vacancy relaxation volume, and c is the vacancy concentration. The thermodynamic variational framework of Gao and Cocks is then used to derive the governing equations for vacancy diffusion [27]:

$$\dot{C} = -\nabla \cdot \mathbf{J} + \dot{C}_{\text{src}} \qquad \text{in } V \tag{III.8}$$

$$\mathbf{J} = -\bar{D}\nabla\mu_v \qquad \text{in } V \tag{III.9}$$

$$\mu_v = \mathbf{t}^0 \cdot \mathbf{n} \qquad \text{on } \partial V \tag{III.10}$$

where $\mathbf{J}$ is the diffusion flux and $\bar{D} = D\Omega c(1-c)/kT$. D is the vacancy diffusion coefficient which is modelled as:

$$D = D_0 \exp\left(-\frac{E_m}{kT}\right) \tag{III.11}$$

where D_0 is the asymptotic value of the D at high temperatures and E_m is the vacancy migration energy. In this formulation, the dislocation cores are "smeared out" in order to make the governing equations computationally tractable without discretizing the dislocation cores, and the resulting vacancy concentration field denoted by C [27]. $\dot{C}_{\text{src}}$ is a term which accounts for the change in vacancy concentration due to the positive or negative climb of dislocations and is given by:

$$\dot{C}_{\text{src}}\ V_g = -b^2 \sum_{i \in V_g} v_c^i \tag{III.12}$$

for a group of parallel edge dislocations, where V_g is the domain containing the dislocations. v_c^i is the climb velocity for dislocation i, which is calculated from the climb component of the Peach-Koehler force and vacancy concentration field as:

$$v_c^i = -\eta \frac{D}{b^i} \left[c_0 \exp\left(-\frac{f_c \Omega}{b^i k T} \right) - C \right] \tag{III.13}$$

where η is a constant of order unity and c_0 is the equilibrium vacancy concentration at a given temperature T, expressed as

$$c_0 = \exp\left(-\frac{E_f}{kT} \right) \tag{III.14}$$

The terms in the square brackets of (III.13) represent the differences between vacancy concentration at the dislocation core and the remote vacancy concentration. The climb velocity is then used to calculate the distance climbed by a dislocation over a given period of time. For additional details on the dislocation climb formulation and derivation, the reader is referred to the dissertation of Keralavarma [26] and the recently published article [27].

III.4 Glide Formulation

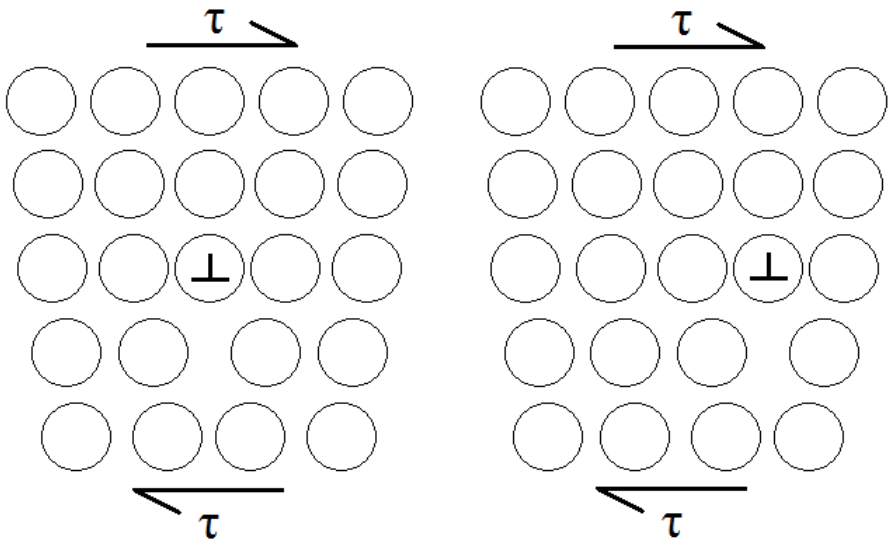

(a) (b)

Figure III.3: Illustration of dislocation glide.

The modeling of dislocation glide utilizes the formulation by van der Giessen and Needleman (1995) with some modifications by Keralavarma [26, 27], the main features of which are summarized here. The driving force for dislocation glide is the component of the Peach-Koehler force along the slip direction, f_g, which is due to the shear stress along the glide direction. The glide of a dislocation is illustrated in figure III.2. This force is used to calculate the velocity of a gliding dislocation v_g^i, which is given by

$$v_g^i = f_g^i / B_g \tag{III.15}$$

where B_g is the drag coefficient on a gliding dislocation due to phonons. Due to the high homologous temperatures associated with dislocation creep, the effect of temperature on the drag coefficient is taken into account through the following equation

$$B_g(T) = B_g^0 T/T_0 \tag{III.16}$$

where B_g^0 is a known drag coefficient at temperature T_0. When two opposite signed dislocations come within a certain distance of each other, they are both destroyed. Dislocations may also become pinned at obstacles randomly distributed over the slip planes. They can become unpinned if the Peach-Koehler force becomes greater than the pinning strength. However, at the higher temperatures at which creep occurs, it is also possible for a dislocation to overcome an obstacle through mechanisms like cross-slip at lower Peach-Koehler forces. To account for this, the probability of a dislocation overcoming an obstacle is calculated as

$$p_{\text{act}} = \exp\left[-\frac{\Delta F}{kT}\left(1 - \frac{|f_g^i|}{\tau_{\text{obs}} b^i}\right)\right] \tag{III.17}$$

where ΔF is the energy required to overcome the obstacle absent the Peach-Koehler force, and $\tau_{\text{obs}} b^i$ is the pinning strength of the obstacle. Additionally, new dislocations can be nucleated from randomly distributed Frank-Read sources. If the Peach-Koehler force is greater than the nucleation stress τ_{nuc} multiplied by the burgers vector over a critical nucleation time t_{nuc}, then a new dislocation dipole is created.

III.5 Simulation Process

For each simulation, an initial microstructure is generated with dislocations, obstacles, and sources randomly distributed on the slip planes in such a way that the total Burgers vector is zero. The initial vacancy concentration field is generated to

correspond to the equilibrium concentration for the applied loading conditions. As mentioned in section III.2, the glide and climb processes are handled separately in order to simulate both in a computationally efficient manner. Additionally not every atomic plane is used for dislocation glide. Instead, active slip planes are created which allow dislocation glide, and which are separated by a specified distance. During the climb process, a climb event is considered to have happened when a dislocation has climbed the distance between active slip planes, at which point it is placed on the new plane. In order for positive climb to occur, a certain number of vacancies, N_v, must be absorbed into the the dislocation core according to

$$N_v = \frac{d_{\text{slp}} b^2}{\Omega} \tag{III.18}$$

where d_{slp} is the distance between slip planes. Negative climb requires that this number of vacancies is nucleated at the dislocation core, which occurs when tensile stresses on a dislocation reach a certain threshold given by

$$\sigma^i b^3 = E_f \tag{III.19}$$

where σ^i is the tensile stress at dislocation i along the Burgers vector. This nucleation and absorption of vacancies is accounted for through the term $\dot{C}_{\text{src}}$ in the governing equation for vacancy concentration, equation III.8.

During the glide process, a time increment of 0.5 ns is used for each time step. On the other hand, when the climb process is being simulated, the time step is 10^{-2} of the estimated time required for a dislocation to climb the distance between active slip planes. This estimate is made by dividing the distance between slip planes by the climb velocity given by equation III.13 where $C = c_0$ and $f_c = 100\sigma b$. The overall

simulation procedure is given by the following iterative process, summarized from [26, 27]:

1. The time step is initialized as the value used for dislocation glide.

2. The initial microstructure is applied to the specimen. Since the dislocation positions are completely random, they are not necessarily arranged in a state of equilibrium. The dislocation glide process is run with no applied stress to relax the stresses on the dislocations and allow them to reach equilibrium positions.

3. Displacements $\pm U/2$ are applied to the faces at $x_1 = \pm L/2$ (see Figure IV.1), and the boundary value problem described in section III.1 is solved to calculate the stress and strain fields. The average stress and strain on the specimen are calculated using [26]

$$\sigma = \frac{1}{D}\int_{-D/2}^{D/2} \sigma_{11}(\pm L/2, x_2)\,\mathrm{d}x_2, \qquad \epsilon = \frac{U}{L} \tag{III.20}$$

   The displacements are incrementally increased and the average stress and strain subsequently calculated until the average stress is equal to the specified creep stress.

4. The Peach-Koehler forces on each dislocation are calculate and the dislocation positions are updated using equation III.15. During this step, dislocations may also be created, pinned at obstacles, or mutually annihilated.

5. Steps 3–4 are repeated until the average strain on the specimen maintains an approximately constant value. This corresponds to the "quasi-equilibrium" state mentioned in section III.2 in which dislocation motion decreases for rea-

sons such as pinning at obstacles. Dislocation motion never truly ceases, so a "quasi-equilibrium" state is considered to have been reached if the average strain rate over the previous 50 time steps falls below a specified threshold.

6. Dislocation glide is suspended and dislocation climb is simulated. The dislocations are held in their positions and the value of the time step is switched to the one used for dislocation climb. The boundary value problem for diffusion is solved using the finite element method. After each time step, the vacancy field is updated and the strain due to the flux of vacancies into or out of the specimen is solved for using

$$\epsilon_d = -\int_0^t \frac{\mathrm{d}t}{LD} \int_{-D/2}^{D/2} \mathbf{J}(x_1 = \pm L/2, x_2) \cdot \mathbf{n} \, \mathrm{d}x_2 \qquad \text{(III.21)}$$

7. The distance climbed by each dislocation is calculated with equation III.13 after each time step and stored. When a dislocation climbs a distance equal to the spacing between active slip planes, the dislocation is moved to the new slip plane.

8. Once climb of a dislocation is detected, the time step is switched back to the value used for dislocation glide and the process begins again with step 3.

CHAPTER IV

PROBLEM FORMULATION

As explained in section I.2, the aim of this work is to expand upon the the work performed by Keralavarma [26] by investigating the effect of varying certain parameters on the creep simulation results. Two parameters of particular interest are the critical climb distance and the vacancy relaxation volume, Ω_v. In the previous work, the critical climb distance was 20 times the burgers vector for all simulations. When setting up a simulation, one could set the critical climb distance so that every atomic plane in along the slip directions in the specimen is modeled. However, it would take much longer to run a simulation as every plane would have to be checked for dislocation activity during each time increment. On the other hand, the distance between slip planes could be so great that there are few slip planes in the specimen. This would reduce the time required to run each simulation, but the physics may not be accurately represented. Additionally, the distance a dislocation is required to climb in order to bypass an obstacle was theorized by Weertman to be one of the factors that determine the steady state creep rate during dislocation creep [39]. It is important, therefore, to determine what effect varying the critical climb distance would have on simulation results.

The other parameter of interest is the vacancy relaxation volume Ω_v, which appears in equation III.7 for the chemical potential of vacancies. In the literature, this property has been reported to be fairly small for aluminum [36]. For this reason, Ω_v was taken to be zero in the simulations performed by Keralavarma. However, this nullifies any effect the hydrostatic pressure would have on the chemical potential of vacancy diffusion through equation III.7, and consequently alters the vacancy diffu-

sion calculations. Accordingly, simulations were performed with a nonzero relaxation volume in order to determine what effect this would have.

In order to investigate the effect of the critical climb distance, creep simulations were run with a critical climb distance of 20 Burgers vectors and a temperature of 400 K at stresses between 10 MPa and 90 MPa. Another set of simulations was run at the same stresses and temperature, but with a critical climb distance of 40 Burgers vectors. To investigate the effect of the vacancy relaxation volume, more creep simulations were performed at the same temperature and stresses with a critical climb distance of 20 Burgers vectors and a vacancy relaxation volume of 10%. For each condition, simulations were run with at least three different initial microstructures.

IV.1 Simulation Setup

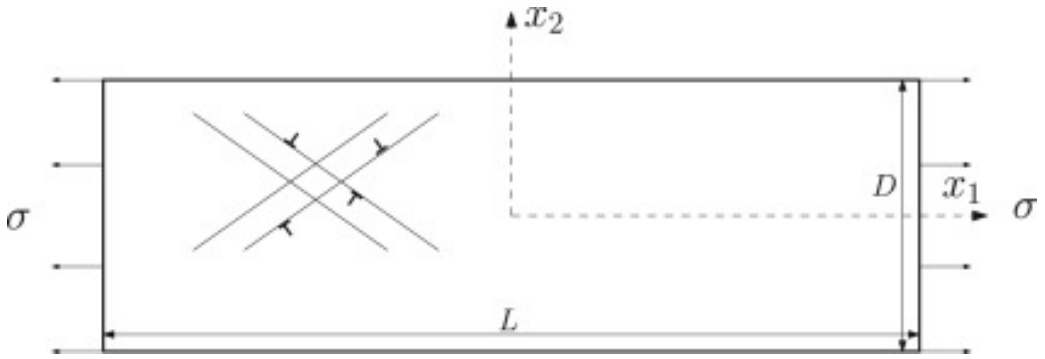

Figure IV.1: Illustration of the specimen used in the creep simulations, reprinted with permission from [27]

Apart from the values of the critical climb distance and vacancy relaxation volume, the simulation parameters are nearly identical to those used in the work by Keralavarma [26, 27], and are described here for completeness. The simulated speci-

men, illustrated in Figure IV.1, is a 12μm by 4μm FCC single crystal with tractions applied to the end faces along the x_1 direction, while the faces normal to the x_2 direction are traction free. There are two active slip systems, which are oriented at $\pm$35.25°with respect to the loading direction. If the loading direction is assumed to be along the $\langle 001 \rangle$ crystallographic direction, then the slip systems relate to the $\langle \bar{1}12 \rangle$ and $\langle 1\bar{1}2 \rangle$ slip directions and the plane of analysis is the (110) plane. The initial densities of the dislocations and sources are $100\mu\text{m}^{-2}$, while the initial obstacle density is $400\mu\text{m}^{-2}$. The nucleation strength of the sources, τ_{nuc} follows a normal distribution with an average of 50 MPa and a standard deviation of 10 MPa. A constant nucleation time, t_{nuc}, of 10 ns is used as well. The strength of the point obstacles, τ_{obs}, is 150 MPa although thermally activated bypass of obstacles at lesser values of the Peach-Koehler force is possible with a probability calculated through the equation III.17.The material properties used for the specimen are the same as those for aluminum and are listed in Table IV.1.

Table IV.1: Material properties used in simulations

Property	Symbol	Value
Young's Modulus	E	70 GPa
Poisson's Ratio	ν	0.33
Burgers Vector	b	0.25 nm
Drag Factor	B_g^0	10^{-4} Pa s (T_0=300 K)
Melting Point	T_M	933 K
Atomic Volume	Ω	16.3 Å^3
Vacancy Formation Energy	E_f	0.67 eV
Vacancy Migration Energy	E_m	0.60 eV
Vacancy Diffusion Coefficient Pre-exponential	D_0	1.51×10^{-5} m^2/s

CHAPTER V

RESULTS

V.1 Effect of Critical Climb Distance

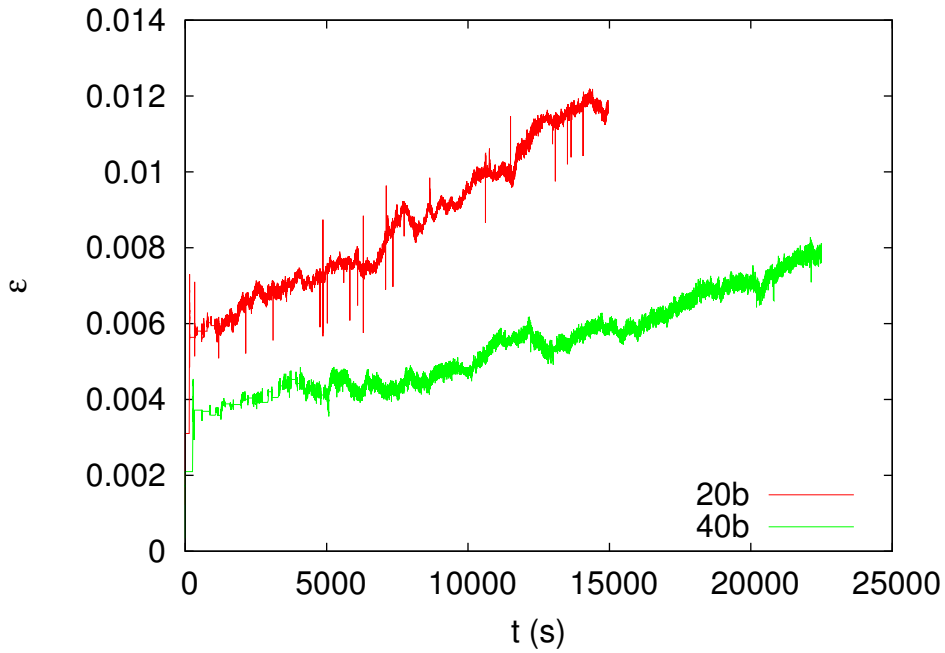

Figure V.1: Plot of strain versus time for an applied stress of 50 MPa

A typical strain versus time response for each critical climb distance at an applied stress of 50 MPa is shown in figure V.1. Each strain versus time graph is characterized by an initial transient followed by a period of steady state creep. One particularly noticeable feature is that the strain rate is greater when the critical climb distance is smaller. In order to quantify this observations, strain rates for each simulation were obtained by fitting a line to the steady state portion of each curve

and recording the slope. The average strain rates for each simulation condition are provided in table V.1, along with ratio of the average strain rate with a critical climb distance of 40 Burgers vectors to the results for a critical climb distance of 20 Burgers vectors (the distance used in the previous simulations by Keralavarma [26, 27]). The strain rate with a critical climb distance of 40 Burgers vectors is approximately half of the rate for a distance of 20 Burgers vectors. However, the strain rates with both critical climb distances range from approximately $10^{-8}s^{-1}$ to $10^{-5}s^{-1}$. Creep rates obtained from experiments on pure aluminum at applied stresses between 10 and 50 MPa range from approximately $10^{-8}s^{-1}$ to $10^{-4}s^{-1}$ [25, 37, 38]. These experiments were performed at a temperature of 473 K, higher than the simulated temperature of 400 K, so a somewhat higher strain rate is expected. Another interesting observation is that for the simulations with a critical climb distance of 40 Burgers vectors, the strain rate was often negative when the applied stress was low. During these simulations, the strain gradually decreased toward zero after the initial rapid increase in strain, as shown in figure V.2 .

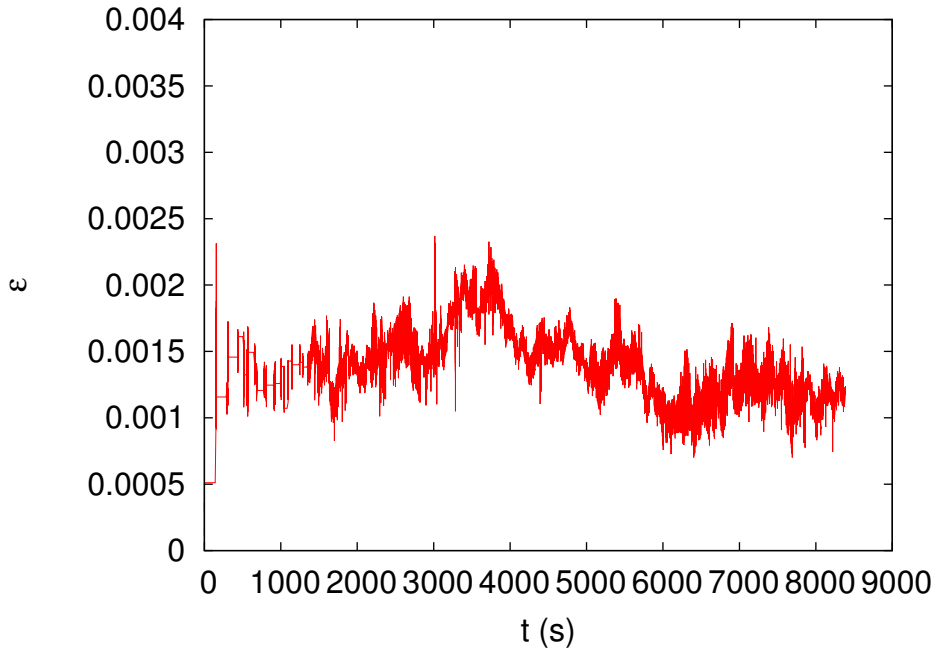

Figure V.2: Plot of strain versus time for an applied stress of 20 MPa. At this relatively low stress, the steady state creep rate is negative.

Table V.1: Average strain rates for each critical climb distance and stress

Stress (MPa)	20b	40b	ratio
10	2.85E-8	-5.28E-9	-0.185
20	4.60E-8	6.81E-8	1.48
30	2.65E-7	1.25E-7	0.470
40	2.29E-7	6.66E-8	0.291
50	3.60E-7	1.42E-7	0.395
60	8.33E-7	2.47E-7	0.296
70	9.87E-7	5.31E-7	0.538
80	3.97E-6	2.80E-6	0.706
90	3.70E-6	1.25E-6	0.338

One other point is that although the applied stress determines the average stress in a simulated specimen, the stress fields due to the position of individual dislocations causes local stress concentrations. These local stress concentrations determine the driving force for each dislocation. The stress field of the ratio of the local stress the x1 direction to the applied stress is shown in Figure V.3. Also shown are contour plots of the total slip accumulated over a period of approximately 3000 s.

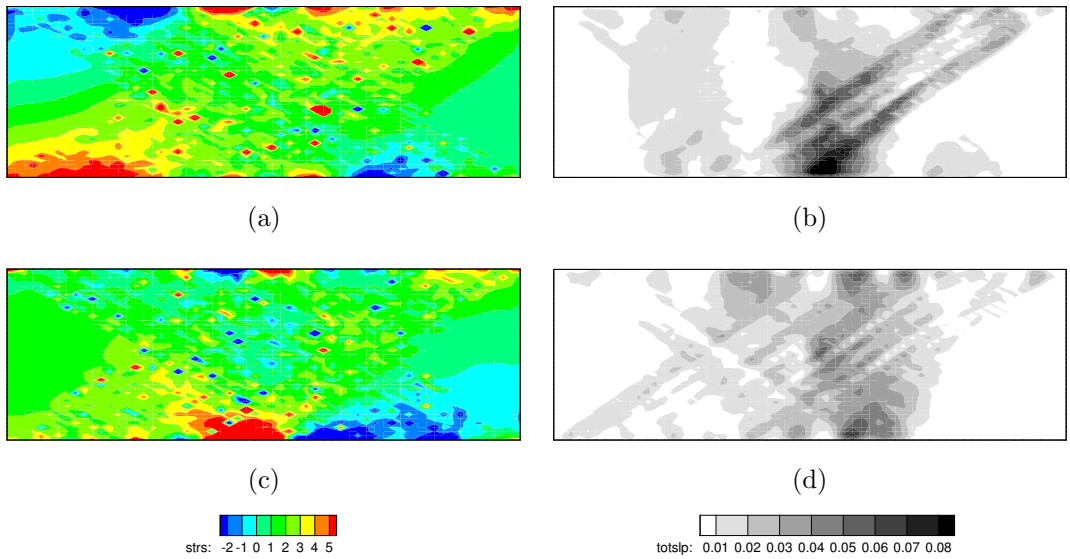

Figure V.3: Contour plots of the ratio of stresses in the x1 direction to the applied stress of 50 MPa (a) and (c) and the slip throughout the specimens. The results for a critical climb distance of 20 Burgers vectors are shown in (a) and (c), while the results for a critical climb distance of 40 Burgers vectors are shown in (b) and (d). The simulated time for the stress plots is approximately 4500 seconds while the slip contours show the slip accumulated over a period of time from approximately 4500 s to approximately 7500 s.

As explained in section II.2, the relationship between applied stress and creep rate is often given by a power law relation of the type $\dot{\varepsilon} \propto \tau^n \bar{d}^{-p}$. In order to compare the effect of critical climb distance on such a relation, the variation of strain rate with stress is plotted on a log-log plot for each value of the critical climb distance, and shown in Figure V.4. The strain rates are plotted versus the shear stress on the slip systems, τ, normalized by the shear modulus, μ. The slope of the plot is then calculated to obtain the value of n. As in the simulations performed by Keralavarma [26, 27], two values of n were calculated, one for higher stresses, and another for lower stresses, possibly simulating the lower stress dependence of Harper-Dorn creep.

The value of n at higher stresses ranges from 7.6 to 7.7, increasing as the distance between slip planes increases. These values are similar to previous results [27]. The experimental value given for pure FCC metals is typically 4-5 [14], although creep experiments on pure aluminum at Temperatures between 400 K and 500 K have given values from 4.4 to 7.6 [25, 37, 38]. The value at lower stresses, on the other hand, ranges from 0.69 to 1.49, similarly increasing as the critical climb distance increases. Interestingly, the lower value of n is not observed in experiments for the applied stress values used in the simulations [38, 37, 25] Despite the effect on creep rates themselves, the critical climb distance does not appear to have any significant effect on the stress dependence of the creep rate.

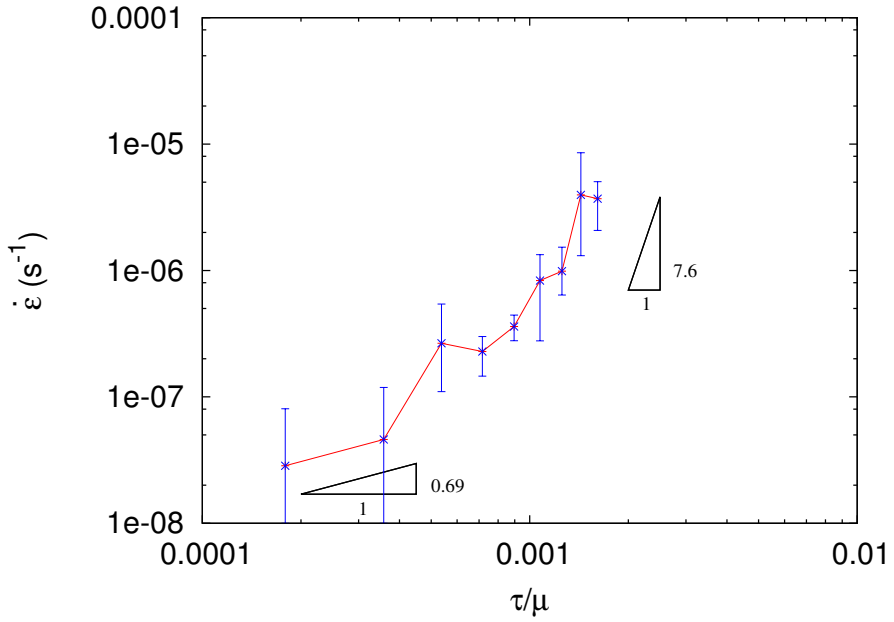

(a)

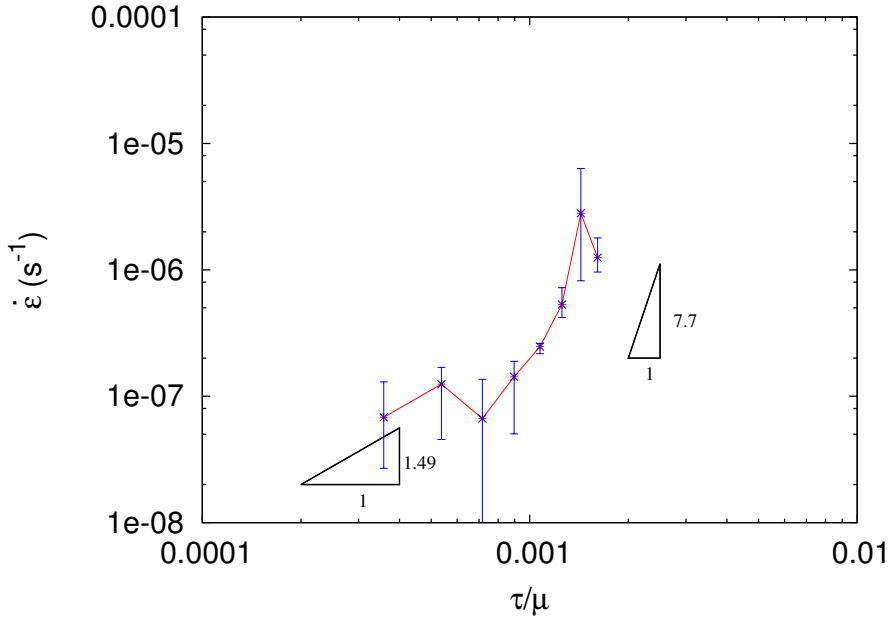

(b)

Figure V.4: Comparison of the variation of strain rate with normalized shear stress for simulations with critical climb distances of (a) 20 and (b) 40 Burgers vectors. The error bars indicate the scatter in results from several different initial microstructures at each stress level. The slope of the curve is the value of the power law creep exponent n.

One final point is that, because the vacancy relaxation volume was omitted, the effect of the pressure gradient is nullified in the calculation of the chemical potential for vacancies (equation III.7), and consequently plays no role in the calculation of the vacancy concentration field, as can be seen in Figure V.5. Although the pressure fields are quite heterogeneous, the vacancy concentration field show much less local variation.

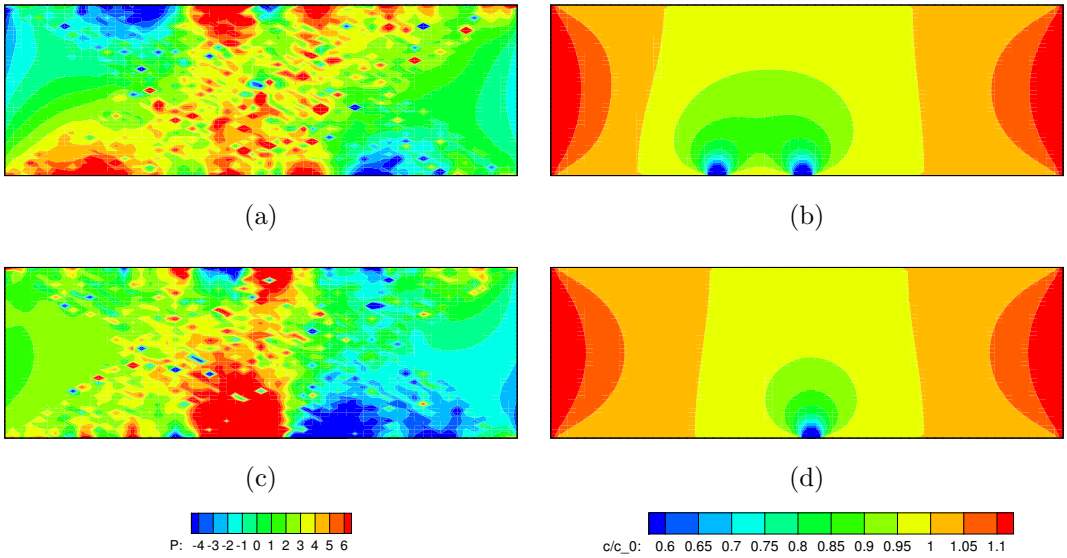

Figure V.5: Contour plots of hydrostatic stress ((a) and (c)) and vacancy concentration ((b) and (d)) for simulations run with an applied stress of 50 MPa and a critical climb distance of 20 Burgers vectors ((a) and (b)) and 40 Burgers vectors ((c) and (d)). All plots show the state of the simulated specimens after approximately 4500 s.

V.2 Analysis of Critical Climb Distance Effect

The creep simulation process is essentially a series of glide steps, during which most of the strain occurs, and climb steps, which resolves the jammed state and allows

further glide to continue. Since the time scale of the glide steps is several orders of magnitude smaller than that of the climb steps, the climb process is the rate limiting step in the simulation of creep. Thus, any effect of the critical climb distance on the time required for a dislocation to climb would directly affect the creep rate. The time required for climb is determined by both the climb distance and the climb velocity, two factors which were also identified by Weertman as directly affecting the dislocation creep rate [39]. Changing the critical climb distance obviously affects the first factor, while analysis of equation III.13, indicates that the climb velocity would be unaffected. Investigation of the time increments used for the climb process during creep simulations shows that increasing the critical climb distance from 20 to 40 Burgers vectors similarly doubles the climb time increment from 12.88 s to 25.77 s, indicating that the climb velocity remains unaffected. Further analysis of the sequence of glide and climb steps for each simulation revealed that the average number of climb events over a 1000 s period of steady state creep was approximately 78 with a critical climb distance of 20 Burgers vectors, and 39 with a critical climb distance of 40 Burgers vectors as shown in Table V.2. Additionally, the total number of time increments (both glide and climb) per 1000 s is approximately reduced by half when the critical climb distance is doubled, while the number of time increments between climb increments remains unaffected. Careful examination of the series of glide and climb steps shows that during the period of steady state a climb event typically occurs precisely every 50 increments and only one climb increment takes place before a climb event occurs, which is the minimum possible. One exception is that, at lower stresses, more glide increments may take place until a jammed state is reached. The explanation for this is that since the glide time increment is only 0.5 ns, the climb steps take up nearly all of the simulated time. Thus, doubling the climb time increment reduces the number of possible climb events by half. For a

period of 1000 s, the maximum possible number of climb events with a climb time increment of 12.88 s is approximately 78, while approximately 39 climb events are possible when the climb time increment is 25.77 s. Therefore, over a given time period a critical climb distance of 40 Burgers vectors only allows half the number of glide increments that are allowed with a critical climb distance of 20 Burgers vectors. This corresponds with the 50% reduction in the creep rate that is observed when the critical climb distance is doubled.

Table V.2: Average number of climb events, time increments, and time increments per climb event over 1000 s of steady state creep for each applied stress and critical climb distance value.

	Climb Events		Increments		Avg. Increments per Climb Event	
Stress (MPa)	20b	40b	20b	40b	20b	40b
10	78	39	4008.5	1960	51.39	50.26
20	78	39	3916.5	2094.7	50.21	53.71
30	78	39	3900	1954	50	50.1
40	78	39	3902.5	1951	50.03	50.03
50	78	39	3900	1950	50	50
60	78	39	3900	1950	50	50
70	78	39	3900	1950	50	50
80	78	39	3900	1917.3	50	50.02
90	78	39	3900	1868.3	50	50.04

V.3 Effect of Vancancy Relaxation Volume

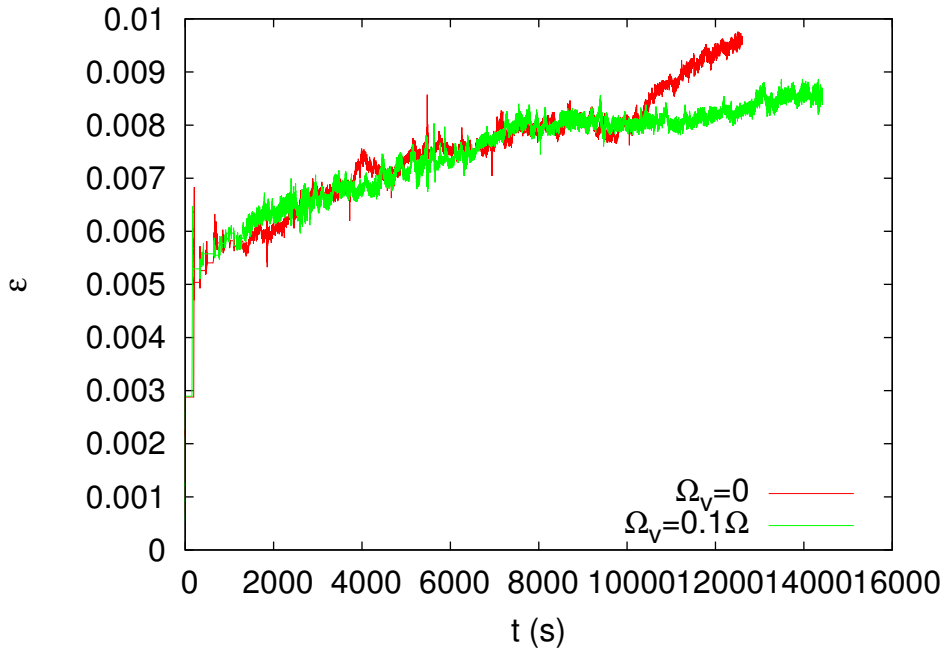

Figure V.6: Plot of strain versus time for simulations with an applied stress of 50 MPa and vacancy relaxation volumes of 0 and 10% of the atomic volume.

In order to determine the effect of using a nonzero value for the vacancy relaxation volume, simulations were run for a temperature of 400 K at applied stresses between 10 MPa and 90 MPa. The critical climb distance was 20 Burgers vectors. A vacancy relaxation volume of 10% of the atomic volume was used and at least three simulations were run at each stress. A stress versus time plot of two simulations at a stress of 50 MPa is shown in Figure V.6. Compared to the simulations with varied critical climb distances, the stress versus time plots with and without a vacancy relaxation volume are qualitatively similar. The average strain rate at each stress is shown in Table V.3, along with the ratio of the value for the case with 10% vacancy

relaxation volume to the value for the case with zero vacancy relaxation volume. Examination of the table does not show as stark of a difference in creep rates as was observed when the critical climb distance was varied, although the the creep rate tends to be lower at high stresses with a nonzero vacancy relaxation volume. Once again, the strain rates are in reasonable agreement with experimental results.

Table V.3: Average strain rates for simulations with zero vacancy relaxation volume and with a vacancy relaxation volume of 10% of the atomic volume. The critical climb distance used was 20 Burgers vectors

Stress (MPa)	$\Omega_v = 0$	$\Omega_v = 0.1\Omega$	ratio
10	2.85E-8	2.95E-8	1.03
20	4.60E-8	8.10E-8	1.76
30	2.65E-7	1.70E-7	0.640
40	2.29E-7	3.01E-7	1.32
50	3.60E-7	2.98E-7	0.827
60	8.33E-7	4.91E-7	0.590
70	9.87E-7	8.51E-7	0.863
80	3.97E-6	1.64E-6	0.414
90	3.70E-6	2.83E-6	0.765

As was done for the simulations with varied critical climb distances, the strain rates for the simulations with a nonzero vacancy relaxation volume were plotted on a log-log scale as a function of the normalized shear stress to determine the power law creep exponent, n. This is shown in Figure V.7(a). The lower stress exponent was found to be 1.69, while the higher stress exponent was calculated to be 4.36, which

is at the lower end of the range obtained from experiments. Compared to the results with a vacancy relaxation volume of zero, there is a smaller difference between the higher and lower stress exponents. Additionally, there is a more uniform increase in strain rate with an increase in stress, and less scatter in the results, particularly at higher stresses. When the two curves are superimposed, as in Figure V.7(b), the curve for the simulations with 10% relaxation volume does not rise as quickly with increasing stress. However, the difference in creep rate is within the scatter of the creep rates from the simulations with zero vacancy relaxation volume, and the difference in the results may be simply due to the random microstructures that were used.

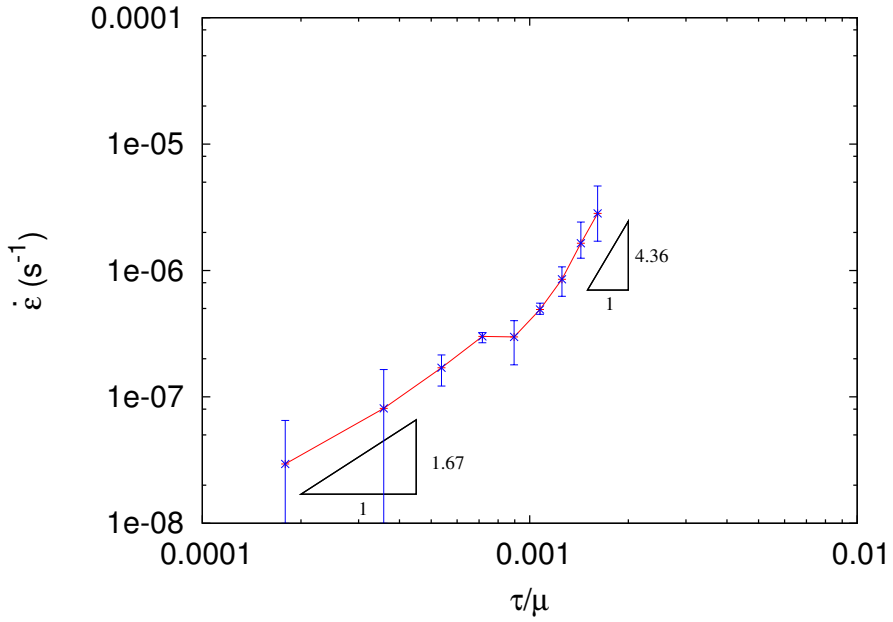

(a)

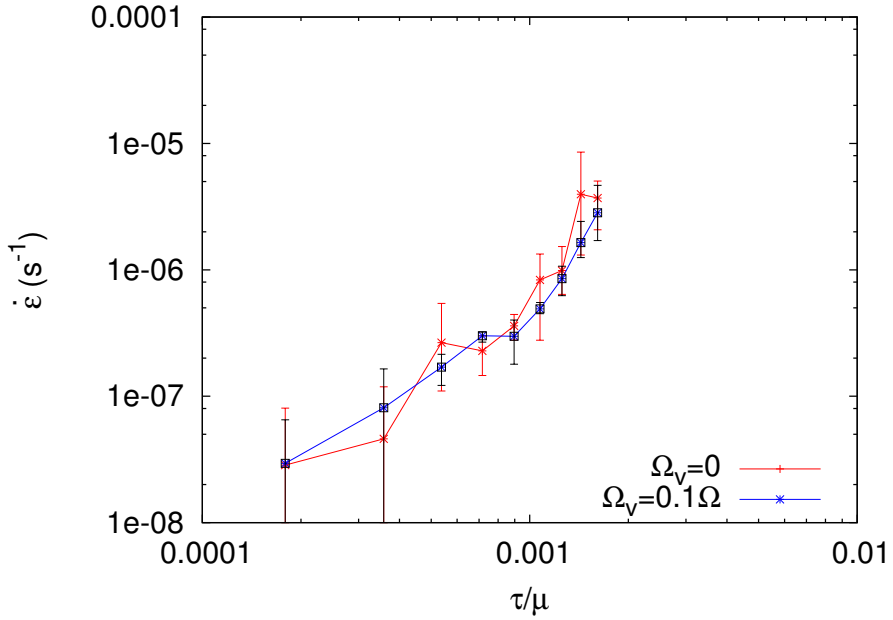

(b)

Figure V.7: (a) Variation of strain rate with normalized shear stress for simulations with a critical climb distance of 20 Burgers vectors and a vacancy relaxation volume of 10%, and (b) the same plot with Figure V.4(a) superimposed for comparison. The error bars indicate the scatter in results from several different initial microstructures at each stress level. The slope of the curve is the value of the power law creep exponent n.

V.4 Analysis of the Vacancy Relaxation Volume Effect

Analysis of the high temperature DD formulation shows that the vacancy relaxation volume parameter enters the framework via the equation for the vacancy chemical potential, Equation III.7. Thus, the value of the vacancy relaxation volume could only affect the vacancy diffusion and dislocation climb parts of creep simulation, and not the dislocation glide portion of creep simulation. As in Section V.2, the number of climb events over a 1000 s period of steady state creep were recorded for each simulation. As was the case for simulations run with zero relaxation volume, there were exactly 78 climb events per 1000 s with approximately 50 glide steps in between each climb step. Additionally, the climb time step increment was exactly the same value for simulations with 0 and with 10% vacancy relaxation volume. This indicates that the vacancy relaxation volume has no effect on the series of dislocation climb and glide steps that govern the simulation of dislocation creep. Consequently, the reason for the difference in creep exponents remains unclear and may simply be due to the difference in the randomly generated microstructures that were used. However, the use of a nonzero vacancy relaxation volume does introduce the effect of the pressure gradient into the vacancy concentration calculation as can be seen by combining equations III.7, III.8, and III.9 and linearizing:

$$\dot{C} = D\nabla^2 C - \frac{D\Omega_v}{kT}\nabla \cdot C\nabla p + \dot{C}_{\text{src}} \qquad \text{in } V \tag{V.1}$$

The effect of the pressure gradient can be clearly seen in Figure V.8. Compared to the vacancy concentration field for the simulation without a vacancy relaxation volume, the vacancy concentration field for the simulation with a 10% vacancy relaxation volume is much more heterogeneous.

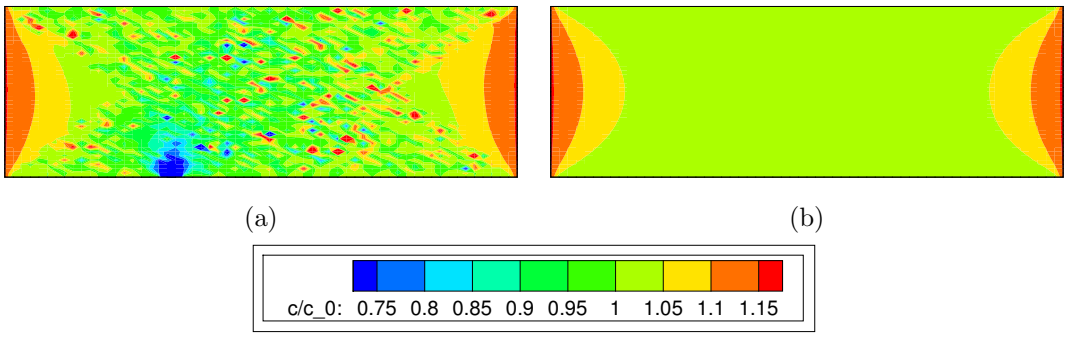

Figure V.8: Contour plots of vacancy concentration for simulations run with an applied stress of 50 MPa and vacancy relaxation volumes of 10% (a) and 0 (b). All plots show the state of the simulated specimens after approximately 4500 s.

CHAPTER VI

CONCLUSIONS

An investigation has been performed to determine the effects of certain parameters on the results of high temperature dislocation dynamics creep simulations. Specifically, the effects of changing the critical climb distance and using a nonzero value for the vacancy relaxation volume on the creep response of micron scale single crystals were recorded and analyzed. The findings are summarized below:

1. Increasing the critical climb distance by a factor of two decreases the steady state creep rate by the same factor. Since the climb velocity is unaffected by the critical climb distance, changing this distance changes the time it takes for a dislocation to climb to a new slip plane. The time scale of dislocation climb is of the order of 10^9 greater than the time scale of dislocation glide, so the vast majority of simulated time represents the dislocation climb phase of the DD framework and any change in the time to climb thus directly affects the steady state creep rate.

2. Changing the critical climb distance has no apparent effect on the stress dependence of the creep rate.This is because the critical climb distance only affects the climb phase of the simulation process and not the glide phase during which most of the strain occurs.

3. Using a nonzero value for the vacancy relaxation volume seems to have a slight effect on the steady state creep rate, particularly at higher stresses where the creep rate is reduced compared to when the vacancy relaxation volume is zero. Correspondingly, the stress dependence of the creep rate was also reduced with

a nonzero vacancy relaxation volume. Although these effects were observed, no apparent cause could be found, and they may simply be due to the variation in the microtructures that were used in the simulations.

4. Running simulations with a nonzero vacancy relaxation volume introduces the effect of the pressure gradient into the calculation of the vacancy concentration field, as can be seen in contour plots of the vacancy concentration.

Further work is still needed in order to enable the use of DD to model and predict TBC failure. In particular, the present framework would have to be extended to simulate creep in polycrystalline specimens and include grain boundary diffusion. Additionally, the ability to simulate the diffusion of anionic and cationic vacancies is necessary in order to simulate the growth of the TGO. Finally, the ability to simulate the mechanical response of multiple layers of different materials would enable a full TBC system to be simulated.

REFERENCES

[1] Size effects under homogeneous deformation of single crystals: A discrete dislocation analysis. *Journal of the Mechanics and Physics of Solids*, 56(1):132 – 156, 2008. Bridging scales in mechanics -.

[2] R. J. Amodeo and N. M. Ghoniem. Dislocation dynamics. i. a proposed methodology for deformation micromechanics. *Phys. Rev. B*, 41:6958–6967, Apr 1990.

[3] D.S. Balint and J.W. Hutchinson. Undulation instability of a compressed elastic film on a nonlinear creeping substrate. *Acta Materialia*, 51(13):3965 – 3983, 2003.

[4] D.S. Balint and J.W. Hutchinson. An analytical model of rumpling in thermal barrier coatings. *Journal of the Mechanics and Physics of Solids*, 53(4):949 – 973, 2005.

[5] A A Benzerga, Y Brchet, A Needleman, and E Van der Giessen. Incorporating three-dimensional mechanisms into two-dimensional dislocation dynamics. *Modelling and Simulation in Materials Science and Engineering*, 12(1):159, 2004.

[6] F.R. Brotzen, C.T. Rosenmayer, C.G. Cofer, and R.J. Gale. Creep of thin metallic films. *Vacuum*, 41(46):1287 – 1290, 1990. Selected proceedings of the 11th international vacuum congress (IVC-11) 7th International Conference on Solid Surfaces (ICSS-7).

[7] D.R. Clarke. The lateral growth strain accompanying the formation of a thermally grown oxide. *Acta Materialia*, 51(5):1393 – 1407, 2003.

[8] H.H.M. Cleveringa, E. Van der Giessen, and A. Needleman. A discrete dislocation analysis of mode i crack growth. *Journal of the Mechanics and Physics of*

Solids, 48(67):1133 – 1157, 2000.

[9] R. L. Coble. A model for boundary diffusion controlled creep in polycrystalline materials. *Journal of Applied Physics*, 34(6), 1963.

[10] E. Van der Giessen, V.S. Deshpande, H.H.M. Cleveringa, and A. Needleman. Discrete dislocation plasticity and crack tip fields in single crystals. *Journal of the Mechanics and Physics of Solids*, 49(9):2133 – 2153, 2001. The {JW} Hutchinson and {JR} Rice 60th Anniversary Issue.

[11] E Van der Giessen and A Needleman. Discrete dislocation plasticity: a simple planar model. *Modelling and Simulation in Materials Science and Engineering*, 3(5):689, 1995.

[12] G.E. Dieter. *Mechanical Metallurgy*. McGraw-Hill, 1986.

[13] A.G. Evans, D.R. Mumm, J.W. Hutchinson, G.H. Meier, and F.S. Pettit. Mechanisms controlling the durability of thermal barrier coatings. *Progress in Materials Science*, 46(5):505 – 553, 2001.

[14] H.J. Frost and M.F. Ashby. *Deformation-mechanism maps: the plasticity and creep of metals and ceramics*. Pergamon Press, 1982.

[15] B. Gleeson. Thermal barrier coatings for aeroengine applications. *Journal of Propulsion and Power*, 22(2):375–383, 2006.

[16] Julia R. Greer and Jeff Th.M. De Hosson. Plasticity in small-sized metallic systems: Intrinsic versus extrinsic size effect. *Progress in Materials Science*, 56(6):654 – 724, 2011. Festschrift Vaclav Vitek.

[17] Julia R. Greer, Warren C. Oliver, and William D. Nix. Size dependence of mechanical properties of gold at the micron scale in the absence of strain gradients. *Acta Materialia*, 53(6):1821 – 1830, 2005.

[18] P.J. Guruprasad and A.A. Benzerga. A phenomenological model of size-dependent hardening in crystal plasticity. *Philosophical Magazine*, 88(30-32):3585–3601, 2008.

[19] S.M. Hafez Haghighat, G. Eggeler, and D. Raabe. Effect of climb on dislocation mechanisms and creep rates in -strengthened ni base superalloy single crystals: A discrete dislocation dynamics study. *Acta Materialia*, 61(10):3709 – 3723, 2013.

[20] J Harper and J.E Dorn. Viscous creep of aluminum near its melting temperature. *Acta Metallurgica*, 5(11):654 – 665, 1957.

[21] Conyers Herring. Diffusional viscosity of a polycrystalline solid. *Journal of Applied Physics*, 21(5), 1950.

[22] Hiroyuki Hirakata, Naomichi Fukuhara, Shoichi Ajioka, Akio Yonezu, Masayuki Sakihara, and Kohji Minoshima. The effect of thickness on the steady-state creep properties of freestanding aluminum nano-films. *Acta Materialia*, 60(11):4438 – 4447, 2012.

[23] J.P. Hirth and J. Lothe. *Theory of Dislocations*. Krieger Publishing Company, 1982.

[24] A.M Karlsson, J.W Hutchinson, and A.G Evans. The displacement of the thermally grown oxide in thermal barrier systems upon temperature cycling. *Materials Science and Engineering: A*, 351(12):244 – 257, 2003.

[25] Megumi Kawasaki, Irene J. Beyerlein, Sven C. Vogel, and Terence G. Langdon. Characterization of creep properties and creep textures in pure aluminum processed by equal-channel angular pressing. *Acta Materialia*, 56(10):2307 – 2317, 2008.

[26] Shyam Mohan Keralavarma. *A Contribution to the Modeling of Metal Plasticity and Fracture: from Continuum to Discrete Descriptions*. PhD thesis, Texas A&M University, 2011.

[27] S.M. Keralavarma and A.A. Benzerga. High-temperature discrete dislocation plasticity. *Journal of the Mechanics and Physics of Solids*, 82:1 – 22, 2015.

[28] D. Kiener, P.J. Guruprasad, S.M. Keralavarma, G. Dehm, and A.A. Benzerga. Work hardening in micropillar compression: In situ experiments and modeling. *Acta Materialia*, 59(10):3825 – 3840, 2011.

[29] Ladislas P Kubin, G Canova, M Condat, Benoit Devincre, V Pontikis, and Yves Bréchet. Dislocation microstructures and plastic flow: a 3d simulation. In *Solid State Phenomena*, volume 23, pages 455–472. Trans Tech Publ, 1992.

[30] J. Lpinoux and L.P. Kubin. The dynamic organization of dislocation structures: A simulation. *Scripta Metallurgica*, 21(6):833 – 838, 1987.

[31] M.-Carmen Miguel, Alessandro Vespignani, Michael Zaiser, and Stefano Zapperi. Dislocation jamming and andrade creep. *Phys. Rev. Lett.*, 89:165501, Sep 2002.

[32] D.R. Mumm, A.G. Evans, and I.T. Spitsberg. Characterization of a cyclic displacement instability for a thermally grown oxide in a thermal barrier system. *Acta Materialia*, 49(12):2329 – 2340, 2001.

[33] K. S. Ng and A. H. W. Ngan. Creep of micron-sized aluminium columns. *Philosophical Magazine Letters*, 87(12):967–977, 2007.

[34] Nitin P. Padture, Maurice Gell, and Eric H. Jordan. Thermal barrier coatings for gas-turbine engine applications. *Science*, 296(5566):280–284, 2002.

[35] M. Peters, C. Leyens, U. Schulz, and W. A. Kaysser. Eb-pvd thermal barrier coatings for aeroengines and gas turbines. *Advanced Engineering Materials*, 3(4):193–204, 2001.

[36] W. Schilling. Self-interstitial atoms in metals. *Journal of Nuclear Materials*, 6970(0):465 – 489, 1978.

[37] V. Sklenicka, J. Dvorak, P. Kral, Z. Stonawska, and M. Svoboda. Creep processes in pure aluminium processed by equal-channel angular pressing. *Materials Science and Engineering: A*, 410411:408 – 412, 2005. The Langdon Symposium: Flow and forming of Crystalline Materials.

[38] V. Sklenika, J. Dvok, and M. Svoboda. Creep in ultrafine grained aluminium. *Materials Science and Engineering: A*, 387389:696 – 701, 2004. 13th International Conference on the Strength of Materials.

[39] J. Weertman. Theory of steadystate creep based on dislocation climb. *Journal of Applied Physics*, 26(10), 1955.

[40] J. Weertman. Creep of polycrystalline aluminium as determined from strain rate tests. *Journal of the Mechanics and Physics of Solids*, 4(4):230 – 234, 1956.

[41] J. Weertman. Steadystate creep through dislocation climb. *Journal of Applied Physics*, 28(3), 1957.

[42] Andreas Widjaja, Erik Van der Giessen, and Alan Needleman. Discrete dislocation modelling of submicron indentation. *Materials Science and Engineering: A*, 400401:456 – 459, 2005. Dislocations 2004An International Conference on the Fundamentals of Plastic Deformation.

[43] Mu Yeh Wu and Oleg D. Sherby. Unification of harper-dorn and power law creep through consideration of internal stress. *Acta Metallurgica*, 32(9):1561 –

1572, 1984.